

Direct Detection of V-V Atom Dimerization and Rotation Dynamic Pathways upon Ultrafast Photoexcitation in VO₂

Junjie Li,¹ Lijun Wu,¹ Shan Yang^{1,2}, Xilian Jin,³ Wei Wang¹, Jing Tao¹, Lynn Boatner,⁴ Marcus Babzien,⁵ Mikhail Fedurin,⁵ Mark Palmer,⁵ Weiguo Yin,¹ Olivier Delaire^{1,2,6} and Yimei Zhu^{1,*}

¹*Condensed Matter Physics and Materials Science, Brookhaven National Laboratory, Upton, New York 11973, USA*


²*Department of Mechanical Engineering and Materials Science, Duke University, Durham, North Carolina 27708, USA*

³*College of Physics, Jilin University, Changchun 130012, China*

⁴*Materials Science and Technology Division, Oak Ridge National Laboratory, Oak Ridge, Tennessee 37831, USA*

⁵*Accelerator Test Facility, Brookhaven National Laboratory, Upton, New York 11973, USA*

⁶*Department of Physics and Department of Chemistry, Duke University, Durham, North Carolina 27708, USA*

 (Received 9 June 2021; revised 1 November 2021; accepted 22 February 2022; published 9 May 2022)

Photoinduced ultrafast phase transitions can generate quasiequilibrium states with novel emergent properties modulated by the interplay of electronic and lattice degrees of freedoms. Therefore, accurately probing transient atomic structures and their dynamics is crucial to understand and control the interaction of electrons and lattice but remains a central challenge of ultrafast science. Using MeV ultrafast electron diffraction on single crystals, we quantitatively reveal the photoinduced lattice distortion of the monoclinic M1 phase of VO₂. Our results resolve previous controversies concerning decoupled distortion components, as well as a proposed M2 intermediate phase. Further, we emphasize the importance of quantifying the transformed phase fraction into the metallic rutile phase, beyond previously reported analyses, and we also clarify the importance of thermal heating in assisting the insulator-metal transition. Our complementary *ab initio* molecular dynamics calculations support the experimental findings and identify the primary A_g phonon mode coupling to photoexcitation. Our study provides the critical and previously missing precise 3D and time-resolved structural evolution of the crystal structure of photoexcited M1 VO₂. These results provide the basis upon which to rationalize this archetypal photoinduced transition.

DOI: [10.1103/PhysRevX.12.021032](https://doi.org/10.1103/PhysRevX.12.021032)

Subject Areas: Condensed Matter Physics
Materials Science

I. INTRODUCTION

The generation and control of novel phases in solids and the understanding of mechanisms underlying their emergent behaviors are at the heart of condensed matter physics research [1,2]. In strongly correlated materials, competing degrees of freedom of charge, spin, orbital, and lattice can be manipulated to engender new properties with ultrafast pump-probe techniques that drive the system far from equilibrium. Ultrafast light pulses can be used to manipulate the dynamic structural response and generate transient

or hidden states arising from intertwined competing phases, e.g., enhanced transient superconductivity (up to 300 K) in YBa₂Cu₃O_{6.5} [3] and topological phase transition in ZrTe₅ [4,5] triggered by photoexcited A_g phonons. However, precisely tracking the electron-lattice coupling via three-dimensional structural characterization of transient states remains extremely challenging, in part because electronic states can respond to minute changes in the lattice and the phenomena are short-lived. Among current pump-probe techniques [6–10] developed to capture dynamical transition pathways, MeV ultrafast electron diffraction (MeV UED) on single crystals stands out for its unique capabilities of providing femtosecond temporal resolution as well as unparalleled sensitivity to atomic positions and displacements through the access to high-order momentum space [10–13].

The insulator-to-metal transition (IMT) in vanadium dioxide (VO₂), driven by an interplay of correlated electrons and strongly anharmonic phonons, holds promise for

*Corresponding author.

zhu@bnl.gov

Published by the American Physical Society under the terms of the [Creative Commons Attribution 4.0 International license](https://creativecommons.org/licenses/by/4.0/). Further distribution of this work must maintain attribution to the author(s) and the published article's title, journal citation, and DOI.

fast and dissipationless resistive switching in neuromorphic computing and memory technologies [14–17]. Despite the intense and sustained interest in the VO₂ IMT, many questions remain open. In previous pump-probe studies of VO₂, short pulses of optical photons, x rays, or electrons have been used to assess the dynamical processes of the photoinduced IMT, including those associated with the electronic structure, displacive lattice evolution, and disordering [8,18,19]. Femtosecond laser excitation (near-IR) above a threshold fluence triggers the transition from the monoclinic (M1) to the rutile (R) phase at temperatures well below the critical temperature $T_c \sim 340$ K of the thermal transition [8,9,18–20]. However, the detailed evolution of atomic distortions and their relaxation pathway during the phase transition are still unsettled, including the respective importance of stretching (dimer breaking) and rotation (twisting) of V-V dimers. Because of the structural and electronic complexity [21–23], with Mott correlation and Peierls distortion coexisting with orbital splitting in the V–V chains, the lack of a detailed structural picture stands in the way of a deeper understanding of the transition mechanism. It has been shown that both depopulation of the V–V bonding orbitals via electron-electron interactions and V–V dimerization distortions contribute to the IMT [21,24]. It was reported that upon photoexcitation, the V atoms rearrange themselves from the original zigzag V-V dimer configuration in the M1 phase into a linear isometric form in the R phase in a two-step fashion, namely suppression of V-V dimerization followed by suppression of the V–V bond rotation [9]. Suppression of correlation-induced splitting of the V-3*d* orbitals of a_{1g} , e_g^π , and e_g^σ and their overlap leads to the insulating band gap collapse [25]. The intertwined nature of lattice kinetics and electronic structure evolution epitomizes how unraveling the time-resolved V-V structural rearrangement is a key factor to achieve a mechanistic understanding of the IMT in VO₂. Additional unanswered critical questions are whether the system is homogeneous or partially excited and transformed, and whether thermal heating plays an important role. Although these issues have remained only tangentially discussed in the literature, we note that most x-ray and electron diffraction experiments reported some remaining intensity for reflections that solely belong to the M1 phase after photoexcitation, revealing a partial IMT transition over the probed volume, even at high pump fluences [8,9,18,19,26].

In this study, we use femtosecond laser pulses to trigger the M1-R transition in single-crystal VO₂ and MeV electron pulses to reveal the lattice evolution. We simultaneously track 40 diffraction peak intensities, positions, and widths, which allows a much more quantitative crystallographic analysis than possible in previous experiments. The ultrafast single-crystal diffraction data acquired in transmission mode reveal detailed correlated motions of vanadium atoms from their initial low-symmetry positions in the

M1 phase toward the high-symmetry positions in the photoexcited state, which leads to the localized V-3*d* valence states and gap closure. We precisely measure the stretching and rotation of V-V dimers in VO₂ under intermediate photoexcitation to assess possible soft phonon modes, as a function of time delays under various photoexcitation fluences. The measurements were carried out at two temperatures (314 K, right below $T_c = 340$ K, and 77 K, well below T_c) to probe the dependence of structural dynamics and shed light on the possible role of thermal heating during the phase transition. To understand the atomic dynamics in a short time regime and cumulative effects from forces, where no lattice heating and M1 to R phase transition exists, *ab initio* molecular dynamics (AIMD) and density functional theory (DFT) calculations were also carried out.

II. EXPERIMENTAL SETUP

Single crystals of VO₂ were grown by a crystallization technique incorporating some aspects of “self-fluxing.” The resulting VO₂ samples are highly ordered single-domain crystals in the R phase and exhibit twin domains in the M1 phase [18]. The sample orientation was first characterized by Laue diffraction. The crystal was then sliced along the [010] direction and thinned to electron (30 keV) transparency using focused ion beam (FIB) with a special approach developed by some of us (see Supplemental Material [27]) to maximize thin area. The thin samples were then characterized using transmission electron microscopy at different temperatures to verify the M1 phase and R phase and its IMT (see Supplemental Material, Fig. S1 [27]).

The photoinduced ultrafast structural response was measured by monitoring the change of intensity of the Bragg peaks of the VO₂ crystal in the reciprocal [010] zone axis and corresponding lattice symmetry. The UED experimental setup at BNL was reported previously [10]. Laser pulses with a duration of 180 fs and wavelength of 800 nm were focused on the sample to trigger the distortion. Precisely synchronized 130 fs pulses of 2.8 MeV electrons are used to probe the thinned freestanding VO₂ crystal with a total area of $\sim 100 \times 50 \mu\text{m}^2$ at desired time delays, and the electron diffraction patterns were recorded with an Andor iXon EMCCD camera. The optical penetration depth of the 800 nm pump laser is ~ 130 nm [28] and the mean-free path of 2.8 MeV probe electrons is ~ 170 nm in VO₂, both of which are larger than our sample thickness [nonuniform thickness mostly ranging from 20 to 100 nm, average thickness of 60 nm, shown in Fig. S1(c) [27]]. Thus, the sample is well pumped and probed across the whole thickness. A pump repetition rate of 5 Hz is used to minimize residual heat on the sample (so that the sample remains in M1 phase before each pump pulse arrives), while pump fluences (up to 16 mJ/cm²) were tuned to vary the strength of the excitations. Measurements were performed with the sample base temperature set to 314 K,

slightly below the equilibrium transition temperature T_c (340 K), as well as 77 K (by liquid nitrogen cooling) to investigate potential heating effects of the photoexcitation.

III. RESULTS

The thermally induced first-order IMT of VO_2 occurs upon heating across the critical temperature $T_c \sim 340$ K. It is associated with a structural transition from an M1 insulating phase (band gap $E_g \approx 0.6$ eV) to R metallic phase. In the M1 structure ($P21/c$), vanadium atoms dimerize and rotate with respect to their coordinates in the tetragonal rutile structure ($P42/mnm$) [29], forming a zigzag structure

along the crystallographic \mathbf{a} axis (monoclinic notation) with alternating V–V bond lengths of 2.62 Å (short bonds) and 3.16 Å (long bonds), as shown in Fig. 1(a). The dimers are also slightly rotated with respect to the \mathbf{a} axis (equivalently the \mathbf{c} axis of the R phase). Related monoclinic phases were also reported, for example, an M2 structure ($C2/m$) occurs upon doping, which features a mixture of dimerized and zigzag V chains [30]. The distortion to M1 on cooling doubles the unit-cell size of the R phase along its \mathbf{c} axis and forms a charge density wave (CDW) sublattice along the rutile \mathbf{c} axis with wave vector $2\mathbf{c}_R$. The M1 and R lattices follow the crystallographic relationship of $[100]_{M1} \parallel 2[001]_R$, $[010]_{M1} \parallel [010]_R$, and $[001]_{M1} \parallel [10-1]_R$. There exists an

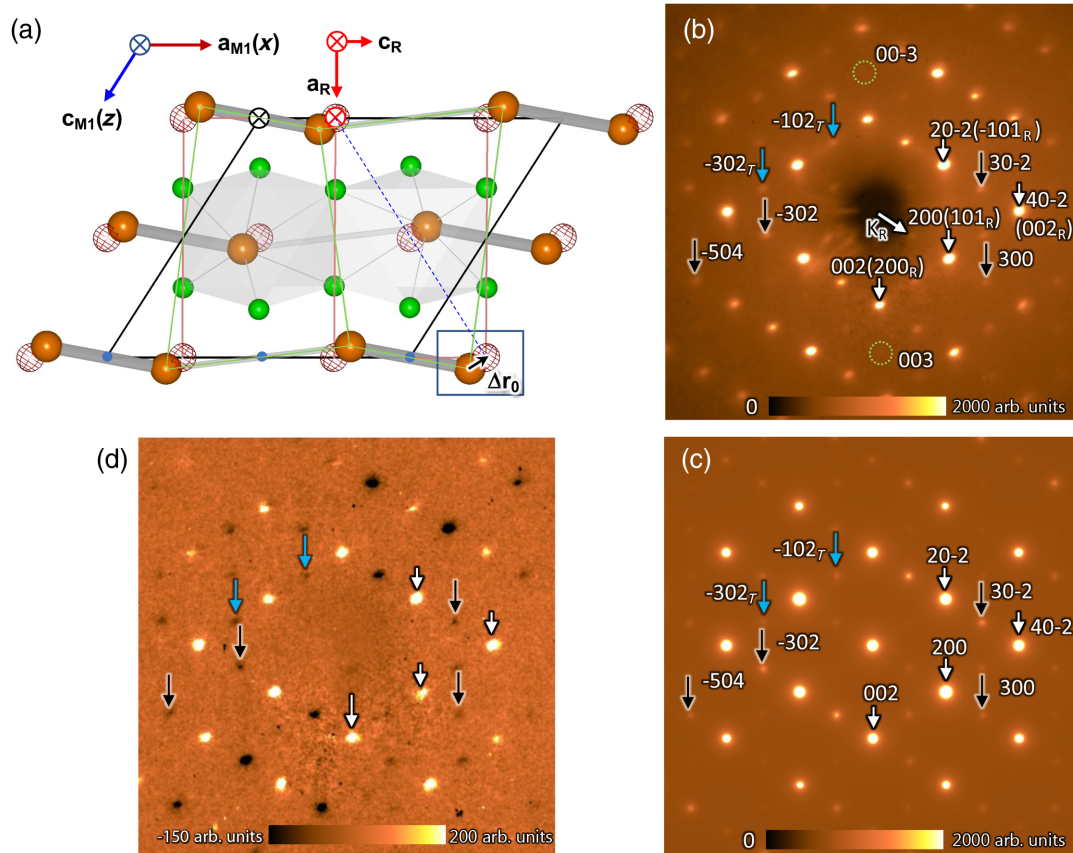


FIG. 1. Structural symmetries and distortions in VO_2 . (a) [010] projection of M1 structure showing V–V bond dimerization (light gray, long bonds; dark gray, short bonds). Solid orange and green balls are V_{M1} and O_{M1} atoms, respectively. V atoms in the R phase are shown in red hollow spheres for comparison. O atoms are not shown due to the overlap with O_{M1} . The inverse center at the middle of each V–V bond is marked by solid blue circles (only the ones at the bottom are shown for clarity). Black parallelogram and red rectangle outline the lattice of M1 and R with their origin labeled by black and red circle cross. $\Delta \mathbf{r}_0$ is the V motion from its M1 to R position marked by the black arrow at the bottom right-hand corner. (b) [010] MeV UED pattern of single crystal VO_2 acquired before time zero at 314 K. The pattern is indexed based on the M1 phase (their R lattice indices shown in parentheses), where the strong spots (hkl with $h = 2n$) indicated by the white arrows are Bragg spots and they appear in both the M1 and R phase. The weak spots (hkl with $h = 2n + 1$), marked by the black arrows, exclusively belong to the M1 phase due to the monoclinic distortion. Other weak spots present, marked by the blue arrows with the subscript T , are due to the (001) reflection twinning. $\mathbf{K}_R = (1/2, 0, 1/2)$ is the wave vector of the M1 superlattice in the reciprocal space of the R lattice. (c) Simulated UED pattern based on dynamic Bloch-wave calculation using the structure model in Refs. [31,32]. (d) Difference pattern of the electron diffraction (the one acquired at 730 ps subtracted that before time zero). The intensity of the Bragg spots (white arrows) increases, while that of the superlattice spots (black arrows) decreases after photoexcitation. Green circles in (b) marked the positions of the possible M2 reflections based on its space group ($C2/m$), which were not observed.

inversion center in the middle of each V–V bond, as marked by a solid blue circle in Fig. 1(a) (only those at the bottom are shown for clarity). The V–V bonding is constrained by these inversion centers; thus the changes of bond geometry can be described by dimer rotation and stretching or shrinking. A wave vector of the M1 superlattice in the reciprocal space of the R lattice is $\mathbf{K}_R = (1/2, 0, 1/2)$ [\mathbf{K}_R is associated with the wave vector of the characteristic soft phonons in Ref. [18], marked by the white arrows in Fig. 1(b)]. The propagation direction of the wave modulation \mathbf{K}_R deviates from $\Delta\mathbf{r}_0$, the direction of V displacement motion [see Fig. 1(a)] from its M1 to R position by 64° . Figure S1(a) depicts the corresponding three-dimensional structural relationship of the M1 and R phases with their structural units outlined.

Figure 1(b) shows a typical MeV UED pattern of VO_2 along the [010] orientation acquired at 314 K, compared with the simulated pattern based on dynamic scattering theory shown in Fig. 1(c) [31]. The pattern is indexed based on the M1 phase, which is composed of two distorted rutile sublattices due to the rotation of V–V dimers (clockwise) and long V–V bonds (counterclockwise) outlined by the green cells in Fig. 1(a). If we ignore the lattice distortion, the sublattices are the same as the R phase lattice, outlined by the red cells. Because of the glide plane symmetry in space group $P2_1/c$, the M1 reflections of $h0l$ with $l = 2m + 1$ (m being an integer), e.g., -301_{M1} , $-10 - 1_{\text{M1}}$, $00 - 3_{\text{M1}}$, and 003_{M1} are absent, as shown in Figs. S1(d) and S2(e) of Supplemental Material [27]. The strong reflections $h0l$ with $h = 2n$ (n being an integer) correspond to the R sublattice and appear in both the M1 and R phase (we denote them as R or primary Bragg peaks). In addition to these strong reflections, much weaker reflections are observed for indices $h0l$ with $h = 2n + 1$, which exclusively belong to the M1 phase due to the monoclinic distortion (we denote them as M1 or superlattice peaks). Opposite rotations of V–V bonds (i.e., dimers counterclockwise and long bonds clockwise) form a (001) reflection twin, yielding reflections, e.g., -102_T and -302_T , as indicated by the blue arrows in Fig. 1(b) and in Fig. S2 of Supplemental Material [27]. Upon photoexciting the M1 phase, V atoms move toward the rutile configuration, suppressing the distortion amplitude of the monoclinic M1 sublattice, and as a result the intensity of the weak superlattice reflections decreases. These reflections eventually disappear when the M1-R transition completes [as observed in our *in situ* heating TEM experiment, Fig. S1(f) [27]]. Concomitantly, the strong ($h = 2n$) reflections become even more intense. Figure 1(d) shows the difference between the MeV UED diffraction patterns recorded at $t = 730$ ps and at $t < 0$. One can observe a clear decrease of the M1 peak intensities and increase of the R peak intensities after photoexcitation.

Figure 2(a) plots the evolution of the averaged intensity for 20 R peaks and 20 M1 peaks as a function of time delay, under a pump fluence of 16 mJ/cm^2 . The pump fluence is

above the threshold but below the saturation fluence for the phase transition reported previously [19], so the focus of our study is more on the lattice dynamics of the M1 phase suppression induced by the photoexcitation rather than the complete M1-R phase transition. The suppression of the M1 distortion or partial melting of its order parameter upon photoexcitation is evident from the simultaneous drop of M1 peak and increase of the R peak intensities, which is similar to the photoinduced suppression of the superlattice in a CDW system. The intensity drop of superlattice M1 peaks in Fig. 2(a) indicates that the structural dynamics consists of a fast process within the first few picoseconds and a relatively slow process that extends to hundreds of picoseconds. The inset of Fig. 2(a) shows the pump-fluence dependence of the intensity change of R and M1 peaks at 730 ps, indicating a $\sim 4.5 \text{ mJ/cm}^2$ threshold for the photo-induced phase transition. The measured peak widths of the M1 and R reflections as a function of time delay are plotted in Fig. 2(b). No change of the peak width is observed within the measurement error in the entire time range. An example of the M1 peak intensity profiles (-104 reflection) at time delay of $t = 0$ ps (black dots) and $t = 730$ ps (open green circles) is shown in the inset of Fig. 2(b). Despite the intensity change with time, the full width at half maximum (FWHM) of the peaks remains unchanged within experiment resolution, suggesting that a single phase remains dominant and the strain gradients are minimal.

Detailed analysis of individual diffraction peaks reveals that the relative intensity change varies among the reflections in two different timescales. The normalized intensity changes of three M1 peaks (for $h0l$, where $h = 2n + 1$, i.e., -104 , 300 , and -504) and three R peaks (for $h0l$, where $h = 2n$, i.e., 004 , -404 , and -604) are plotted in Fig. 2(c). For instance, the intensity drop of the -104 reflection is larger than other reflections and the amplitudes of intensity change in the first and second stage are similar, while the intensity of the 300 peak drops very little in the second stage compared to the first stage. We also found that the intensity of these reflections is sensitive to the V atom displacement with the $\{300\}$ family reflections sensitive to the displacement along the x (\mathbf{a} axis) direction, Δx , and the $\{-104\}$ family reflections mostly to that along the z (\mathbf{c} axis) direction, Δz . For the R peaks, the intensity increases concurrently with the decrease of the M1 peaks, around 15% for -404 and 5% for 004 (first stage) and relaxes to constant (second stage). Meanwhile, increase of the Debye-Waller (DW) factor due to laser-induced thermal motion suppresses the intensity of both M1 and R peaks. Compared to the incoherent deviation from average (long-range) crystalline order revealed by x-ray diffuse scattering [18], this study focuses on the coherent lattice displacement and quantification of the distortion path of average crystal structure by tracking many Bragg peak intensities quantitatively.

In order to understand the directional atomic motions (Δx and Δz) that result in the temporal intensity evolution

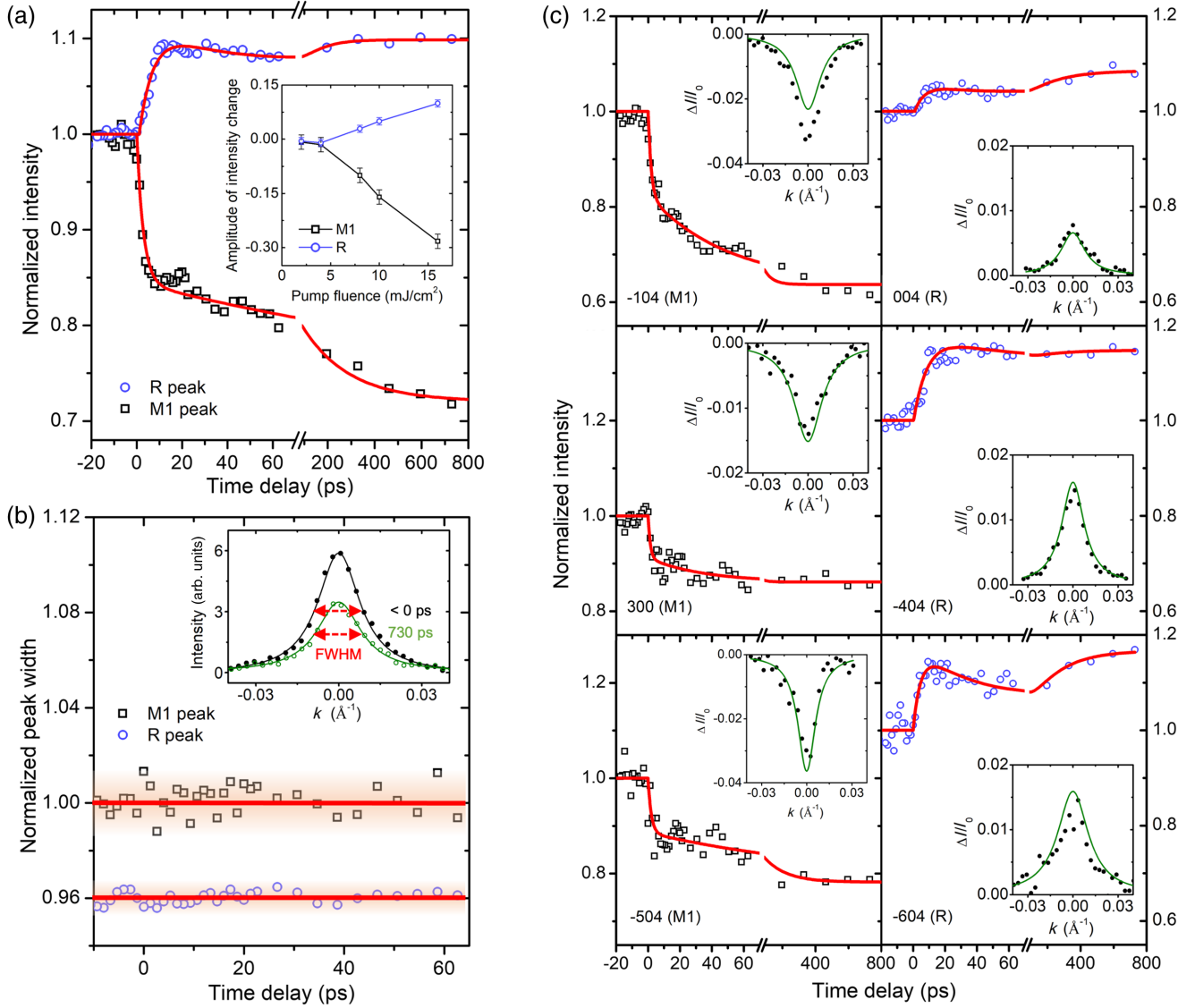


FIG. 2. Photoinduced lattice dynamics. (a) Normalized relative intensity changes of the R peaks (averaging over -402 , -202 , 002 , 202 , -604 , -404 , -204 , 004 , 200 , 400 reflections) and M1 peaks (averaging over -104 , 300 , -302 , -304 , -506 , -504 , -102 , -306 , 102 , -502 reflections) during the photoinduced structural evolution under pump fluence of 16 mJ/cm^2 . The simultaneous increase of R peak and decrease of M1 peak intensity clearly indicate the suppressing of M1 phase upon photoexcitation. Inset: normalized intensity changes of M1 and R peaks as a function of fluence at 730 ps . (b) The averaged peak width of the M1 and R reflections over time, no visible change is observed. Inset: intensity profile of M1 peak (-104) at time delay $t = 0 \text{ ps}$ (black dots) and $t = 730 \text{ ps}$ (open green circles). The solid lines are fitting curve based on the Lorentzian function. Although the peak intensity decreases at $t = 730 \text{ ps}$, the peak width (FWHM) remains constant compared to that at $t = 0$. (c) Temporal evolution of normalized intensity of various M1 peaks ($h0l$ with $h = 2n + 1$) and R peaks ($h = 2n$) averaged over symmetry allowed reflections ($-h0l/h0 - l$ and $h0 - l/-h0l$) under pump fluence of 16 mJ/cm^2 . The red curves are guides to the eyes based on fitting with a double or triple exponential function. All the data shown in (c) were carried out at base sample temperature of 314 K . The measurement errors of normalized peak intensity change, mostly due to shot-to-shot variation of electron beam intensity, are 0.02 (300), 0.02 (-104), 0.03 (-504), 0.009 (004), 0.018 (-404), and 0.015 (-604) (reflection index is indicated in parenthesis), with an integration of 700 shots at each time delay. For clarity, the measurement errors are not plotted in the figure. Insets: quantitative comparisons of normalized experimental (solid dots) and calculated (green curves) intensity changes at 730 ps for the major M1 and R peaks. The calculations are the best fit to the displacement along the \mathbf{a} and \mathbf{c} axes and the Debye-Waller factors obtained from the experiment.

of the M1 and R peaks, we calculate the structure factors of these reflections, which are directly proportional to the square root of the intensities ($I_{h0l} \sim |F_{h0l}|^2$). Given the fact

that the contribution of the oxygen displacement in the two phases (M1 and R) to the diffraction intensities is much smaller than that of V, we for simplicity neglect the

contribution of O atoms in the calculations. The intensity I_{hkl} ($l = 2n$) is therefore

$$I_{h0l} \sim |F_{hol}|^2 = |4f_V \cos[2\pi(hx + lz)] \exp(-Bs^2)|^2, \quad (1)$$

where s is the scattering vector. Note that the imaginary terms are canceled out due to the inversion center symmetry of the M1 phase. By ignoring high-order terms, the normalized intensity change is

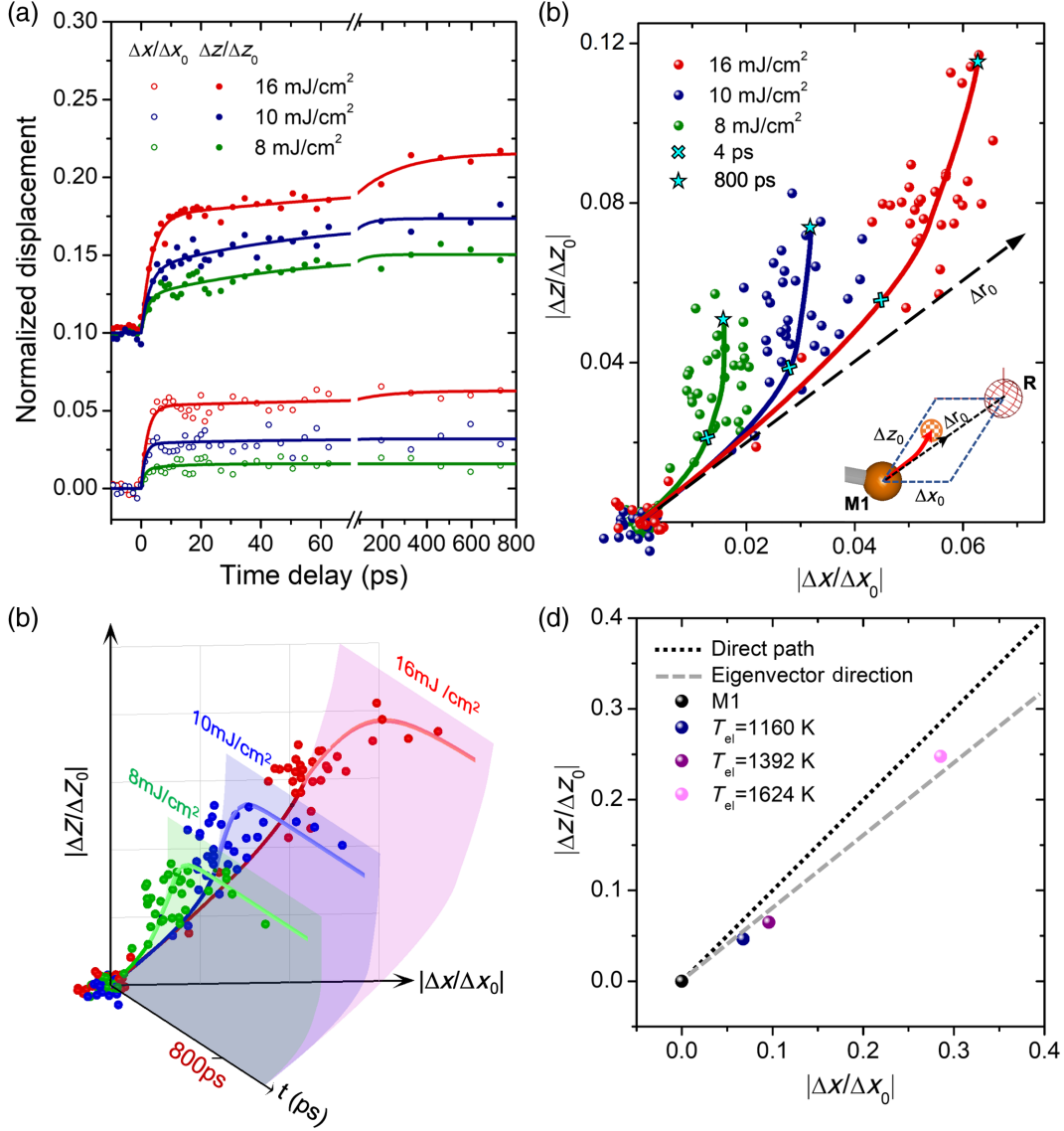


FIG. 3. Correlated vanadium movement upon photoexcitation. (a) The normalized displacement along x and z direction ($|\Delta x/\Delta x_0|$ and $|\Delta z/\Delta z_0|$) as a function of time delay. The displacement along z is shifted vertically for clarity. (b) A 3D plot of the V displacement induced by photoexcitation as a function of time and fluence. Three color planes are the curved surfaces of the vanadium movement plotted along time axis ($t = 0$ –800 ps) for three different fluences. (c) Normalized displacement $|\Delta x/\Delta x_0|$ versus $|\Delta z/\Delta z_0|$ for different time delays projected along the time axis from the 3D plot in (b). The black dashed line indicates the direction of V movement from its M1 to R position. Note for clarity the x and z axes are drawn orthogonally. The actual angle between the two is 57.4° (see inset). The V movements in the first few picoseconds are along the $\Delta \mathbf{r}_0$ direction. The locations of 4 and 800 ps are marked in the fitting curve. With the increase of time delay, the weight of displacement along the c axis increases, significantly departing from the $\Delta \mathbf{r}_0$ direction. Inset: the definition of Δx_0 , Δz_0 , and $\Delta \mathbf{r}_0$ [see the rectangle box in Fig. 1(a)]. The black arrow points to the straight line path of the V atom from the M1 position to the R position. The red line depicts the motion path of V atom under the fluence of 16 mJ/cm² with the end point being at $t = 730$ ps. (d) Calculated $|\Delta x/\Delta x_0|$ versus $|\Delta z/\Delta z_0|$ plot using four parallel AIMD trajectories at different electronic temperature T_{el} . The average V atomic positions between -500 and 0 fs before photoexcitation at 300 K in the AIMD calculations is the origin $(0, 0)_{M1}$. The relative displacements rely on the T_{el} . $|\Delta x/\Delta x_0|$ and $|\Delta z/\Delta z_0|$ at $T_{el} = 1160$ K agreed well with experimental displacement at 4 ps under the fluence of 16 mJ/cm².

$$\Delta I_{h0l}/I_{h0l}^0 \approx -4\pi \tan[2\pi(hx_0 + lz_0)](h\Delta x + l\Delta z) - 2s^2\Delta B, \quad (2)$$

where I_{h0l}^0 , x_0 , and z_0 are the intensity and position of V before photoexcitation ($x_0 = 0.23947$ and $z_0 = 0.02646$ [32]). Δx , Δz , and ΔB are displacement of V along **a** and **c** direction and change of DW factor, respectively. Based on Eq. (2) it is clear the change of diffraction intensities strongly depends on atomic displacements along the **a** and **c** axis. For instance, the intensity changes of 300, -104 , 004, and -404 peak corresponding to the vanadium displacements (Δx and Δz) can be expressed as

$$\begin{aligned} \frac{\Delta I_{300}}{I_{300}^0} &= -187.43\Delta x - 0.19\Delta B, \\ \frac{\Delta I_{-104}}{I_{-104}^0} &= -14.01\Delta x + 56.04\Delta z - 0.31\Delta B, \\ \frac{\Delta I_{004}}{I_{004}^0} &= -39.42\Delta z - 0.39\Delta B, \\ \frac{\Delta I_{-404}}{I_{-404}^0} &= 67.35\Delta x - 67.35\Delta z - 0.338\Delta B. \end{aligned}$$

After photoexcitation, the V atom is expected to move toward the R position ($x_R = 0.25$ and $z_R = 0$), resulting in $\Delta x > 0$ and $\Delta z < 0$; thus the intensity of M1 reflections (e.g., 300 and -104) decreases while that of R reflections (e.g., 004 and -404) increases, depending on the competition between the displacements (Δx and Δz) and the Debye-Waller factor (ΔB). Using the singular-value-decomposition method we achieve the best fit Δx , Δz , and ΔB from the intensity changes of a total of 40 reflections (20 M1 and 20 R reflections) at each time delay during the photoinduced dynamical process. The random thermal vibrations of V atoms based on the measurements of corresponding DW factors are presented in Fig. S5 of Supplemental Material [27].

The normalized V displacements $|\Delta x/\Delta x_0|$ and $|\Delta z/\Delta z_0|$, as a function of time delay under various pump fluences, are shown in Fig. 3(a), clearly illustrating a two-stage dynamic behavior. Δx_0 and Δz_0 are the displacements from M1 position to R position along \mathbf{a}_{M1} and \mathbf{c}_{M1} axes, respectively, in Fig. 3(c) inset. The corresponding path of atomic motion is shown as a function of time delay in Fig. 3(b). The uncertainty (or statistical deviation) of refined $|\Delta x/\Delta x_0|$, $|\Delta z/\Delta z_0|$, and ΔB depends on the measurement error of intensity change of various peaks in Fig. 2(c) and in Fig. S3 [27]. The measurement error of normalized peak intensity change, mostly due to shot-to-shot variation of electron beam intensity, ranges from 0.004 for -204 reflection to 0.034 for -502 reflection with an integration of 700 shots at each time delay. Based on the measurement errors of 20 M1 and R peaks, the standard deviations of $|\Delta x/\Delta x_0|$, $|\Delta z/\Delta z_0|$, and ΔB are calculated to

be ± 0.008 for $|\Delta x/\Delta x_0|$ and $|\Delta z/\Delta z_0|$ and ± 0.01 for ΔB , which are in line with standard deviations of the data points before time zero shown in Fig. 3(a) and in Fig. S5 of Supplemental Material [27].

The V atom motion path as a function of $|\Delta x/\Delta x_0|$ versus $|\Delta z/\Delta z_0|$ is shown in Fig. 3(c). We note V atoms move very fast in the first few picoseconds (first stage) and then slow down (second stage) till its quasiequilibrium position at ~ 800 ps. The larger of the fluence, the faster the movement. Moreover, V atoms move basically along the M1-R line in the first stage. The atomic movement along **x** and **z** directions is linear, thus the ratio $\Delta x/\Delta z$ is a constant, equal to $\Delta x_0/\Delta z_0$ and independent of time delay. The dissociation (elongation) of V-V dimers during the evolution from M1 to R can be represented by the displacement Δx along \mathbf{a}_{M1} , and the untwisting (or derotation) is mostly captured by Δz along \mathbf{c}_{M1} , as depicted in Fig. 1(a). Thus, both dissociation and untwisting of V dimers are heavily involved in the first stage.

With the increase of time (second stage), V movement gradually deviates from the straight line along $\Delta \mathbf{r}_0$. Cyan crosses in Fig. 3(c) mark the points of 4 ps as references to show the timing of the deviation from the M1-R ($\Delta \mathbf{r}_0$) line in the fitting curve and cyan stars mark the points at 800 ps when deviation reaches its quasiequilibrium limit. This suggests that the V displacement has mainly Δz component in the second stage and substantially deviates from its linear pathway from its M1 position to R position, indicating a dominant untwisting of V-V dimer other than dissociation during the slow process. It corresponds to observations that during the first (second) stage, the intensity change of various M1 peaks is significantly different, ranging from 10% (4%) for Δx sensitive {300} to 18% (19%) for Δz sensitive { -104 } reflections.

III. DISCUSSION

A. Atomic pathway of the photoexcited lattice

Photoinduced structural dynamics in VO_2 has been investigated using various pump-probe techniques [8,9,18–20], and most research efforts have focused on the dynamic process in the first few picoseconds. Morrison *et al.* [19] studied polycrystalline films of VO_2 using ultrafast electron diffraction at 95 keV. They observed the evolutions of M1 and R peak intensities upon photoexcitation with two-timescale dynamics (0–1.5 and 2–10 ps) for different V–V bonds based on a pair-distribution-function analysis. The fast and slow components were attributed to the distinct transition occurring in different crystallites in their polycrystalline sample. On the other hand, using 30 keV electrons in a surface-sensitive reflection mode Baum and co-workers probed about 10 atomic layer deep from the surface of single-crystal VO_2 [9] and observed two distinct timescales, $t_1 = 300$ fs and $t_2 = 9$ ps, with V displacement along the **a** axis and **c** axis,

respectively. It showed a different two-stage behavior: the V-V dimerization was first suppressed and then the V-V bond rotation was suppressed. The directions of the displacement were derived based on the intensity analysis of two separate groups of hkl reflections, corresponding to either $h \neq 0$ or $h = 0$. Although their early experiment is admirable, it is largely qualitative with no distinction between the M1 reflections and the M1 + R reflections, and no consideration of DW factors, which are particularly sensitive to the intensities of high-order reflections accessible in the reflection mode. For instance, the contributions of DW factor and displacement along the \mathbf{c} axis to the peak intensity for reflections $h = 0$, say, the 091, 084, and 08-2 reflections discussed in their paper, go to the opposite direction; thus one cannot make a conclusion that there is no displacement if the intensity does not decrease or remains constant. In contrast, in our analysis, we simultaneously refine all reflections with DW factors included. We unambiguously show that during the first stage (2 ps timescale) of the structural dynamics, displacements (dimerization and rotation of V-V bonds) occur along the M1-R line, i.e., along both \mathbf{a}_{M1} and \mathbf{c}_{M1} axes. If we combine the fast and slow time constants in the study of Baum *et al.*, their observations would better agree with our analysis. Our findings not only reveal that the role of stretching A_g phonon mode is limited in the fast dynamics, but also illustrate the dominant and unrevealed role of the rotation A_g phonon mode in the rest of the structural excitation and relaxation in VO_2 .

The previously reported behavior of decoupled dimerization and twisting in two timescales [9] was supported by first-principles calculations based on a separate initial-force treatment of hole doping and electron doping, which found that hole doping favors suppression of the V-V dimerization and electron doping favors the suppression of the V-V bond rotation [33]. Thus, it was speculated that the effects of hole doping and electron doping dominate over different time domains [33]. However, the photoinduced electron excitations create both holes and electrons; therefore, it is necessary to perform first-principles simulations consistent with this physical process and beyond the initial-force approximation. After initial ~ 100 fs (which is time zero of our simulation), the hot electrons relax to a quasithermal distribution corresponding to an elevated electron temperature T_{el} , which is much higher than the lattice base temperature. Subsequently, optical phonons are more likely to be excited by the relaxing electrons than acoustic phonons, yielding a nonthermal distribution of phonons [18,34–37].

We performed *ab initio* molecular dynamics calculations to investigate the atomic motions and unveil the underlying factor that controls atomic motions under photoexcitation. We simulated the laser pumping by suddenly increasing T_{el} and changed the ensemble from canonical to microcanonical [18] (for details, see Note 8 in Supplemental

Material [27]). The AIMD calculations for 1 ps after photoexcitation (1 fs time step) show minimal lattice heating and no complete transition from M1 to R phase. Through averaging the atomic displacement, we reproduce the experimental trend of the atomic path within the first picosecond. First, the average displacement is found to closely follow the M1-R line within 1000 fs [Fig. 3(d)], in agreement with our experiment results. As T_{el} increases from 1160 to 1624 K, the average displacement increases from around 0.1 to 0.3 of total displacements along both Δx_0 and Δz_0 directions [Fig. 3(d) and Supplemental Material Fig. S9 [27]], even though the phase transition does not occur at $T_{el} < 2900$ K (Fig. S7). We further show the importance of the cumulative atomic forces, besides initial forces or velocities, in determining the atomic motions over this timescale.

Next, we extracted the forces and velocities from AIMD to understand the driving factor of the atomic motion. The atomic motion after photoexcitation ($t > 0$ fs) is governed by two factors, the initial configuration and velocity of atoms and the forces acting on them (potential energy surface) [38]. Based on our AIMD over short timescales (1 ps), the velocities of V atoms minimally increase after photoexcitation, which is compatible with negligible lattice heating. With little impact of increasing T_{el} on the velocities from 1160 to 1624 K [Fig. S10(a) [27]], V atom velocities do not lead to the variation of displacements observed in Fig. 3(d). Meanwhile, the average restoring forces after photoexcitation slightly decrease, the more so as T_{el} rises from 1160 to 1624 K [Fig. S10(c) [27]]. Within the first picosecond, the lattice heating is negligible. The kinetic energy and aggregated forces resulting from increased T_{el} are insufficient to overcome the energy barrier between M1 and R phases. Thus, the increased distortion of the M1 phase after 1 ps with increasing T_{el} can be mainly understood as the more efficient channeling of the atoms by shaping the minimum energy path in the potential energy surface.

We now consider the potential energy surfaces to investigate the initial and restoring forces under photoexcitation. The restoring force describes the force that atoms experienced in the photoexcited potential. The initial force corresponds to the force strictly at 0 fs after photoexcitation, when atomic positions have not yet adjusted to photoexcitation. In Fig. 4(a), the position of the energy minimum moves towards R phase ($\Delta d = 0$ Å) by 0.03 Å as T_{el} rises from $T_{el} = 290$ K to $T_{el} = 1624$ K. Additionally, the potential energy surface becomes flatter with increasing T_{el} ; thus the average restoring force decreases. The first-order derivative of the potential energy surface (Fig. S8 of Supplemental Material [27]) corresponds to the restoring forces, which confirms the deviation of restoring forces at $T_{el} = 1160$ –1624 K from that of M1 at $T_{el} = 290$ K. Upon increasing T_{el} , the potential becomes shallower [see Fig. 4(a)] and the restoring forces on V atoms in

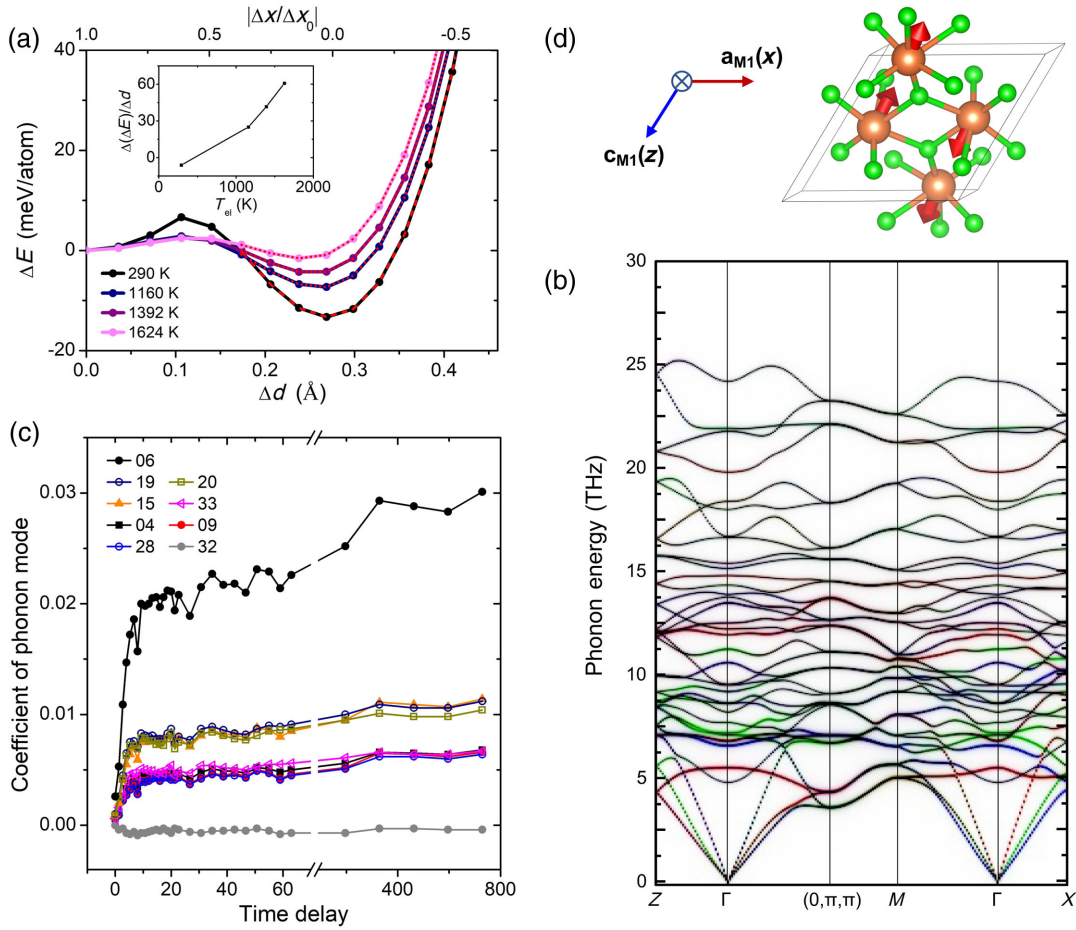


FIG. 4. DFT calculations of various phonon modes in VO_2 . (a) Potential energy surface as structure distorts from M1 to R phase at different T_{el} . Δd is the difference between d_{short} (d_{long}) and the relaxed rutile V-V $d = 2.78 \text{ \AA}$. $\Delta d = 0.27 \text{ \AA}$ corresponds to the relaxed M1 structure, and rutile structure is at $\Delta d = 0 \text{ \AA}$. Raising T_{el} lifts the energy of M1 structure and flattens the potential energy surface. The potential energy surface flattening corresponds to the decreasing forces on atoms and the lowest energy structures transforming toward R phase. The dashed lines are fourth-order polynomial fit. Inset: the forces at $d = 0.27 \text{ \AA}$ from $T_{el} = 290 \text{ K}$ to $T_{el} = 1624 \text{ K}$, corresponding to first-order derivative of polynomial fit of the potential energy surface. (b) The phonon dispersion of VO_2 , where the colors denote contributions from the V atomic vibration along the crystallographic a (red), b (green), and c (blue) directions. (c) Decomposition of the lattice displacement obtained in Fig. 3(a) into the nine A_g Raman phonon modes, drawn in Fig. S4 of Supplemental Material [27]. (d) A schematic of phonon mode 6, which is found to be dominant in the structure transition. The V and O atoms are orange and green balls, respectively. The red arrows represent V displacements. The length of arrows indicates the amplitude of displacement, which are scaled up by a factor of 24.

the photoexcited potential become weaker (Fig. S8 [27]). We also note that at the equilibrium $\Delta d = 0.27 \text{ \AA}$ corresponding to the initial M1 configuration (vertical dashed line in Fig. S8 [27]), the initial force on V atoms increases with the photoexcitation fluence (T_{el}), shown in the inset of Fig. 4(a).

But the restoring forces along the M1 -R path are not constant (Fig. S8 [27]), but rather depend on position d as well. The restoring forces [$f(t)$] vary as the atoms move toward the minimum of the potential energy surface at corresponding T_{el} . Hence, the initial force right after photoexcitation (at $\sim 0 \text{ fs}$) is not the sole factor determining the dynamic process of structural evolution. Instead, the

cumulative effect from restoring forces $f(t, d)$ govern the atomic motions after photoexcitation, as clarified by our AIMD simulations.

Because of limited computation power, we cannot extend the AIMD calculation beyond a few picoseconds and compare with the experiment observation of z direction dominant displacement in the second stage. However, we performed first-principles crystal structural relaxation for various T_{el} to probe the motion of atoms in the photoexcitation experiment. The results show that a non-proportional displacement along the a and c directions occurs at larger T_{el} when approaching the critical value (about 2900 K) of M1-R phase transition [Fig. S7(b) of

Supplemental Material [27]]. A full theoretical understanding and reproducing of the experimental observations remains challenging but may be achieved by extending the AIMD simulation to 1000 ps with consideration of new physics and enhanced computation power in the future [35].

Importantly, the observed atomic pathway provides new insights into the possible phonon modes involved in the structural response of the M1 phase upon excitation by 1.55 eV photon pulses. The transient electronic states and atomic positions of the crystal highly depend on the phonons' involvement in the structural dynamics process. The M1 to R phase transition is widely attributed to the softening of two A_g phonon modes of the M1 phase. The dimerization and rotation of the V—V dimer bond corresponds to the stretching and rotation modes of A_g phonons, respectively. However, the relative importance of these two phonon modes during photoexcitation, in terms of their weight in the phonon population and simultaneity in excitation, has remained unclear. Our results unveil the atomic transition pathway and could advance our understanding of the role played by different phonon modes during photoexcitation. As shown in Fig. 3(c), at each applied pump fluence above the threshold of around 4.5 mJ/cm², the pathway of the first process (fast stage) is mostly along the straight line from M1 to R positions and the amount of displacement increases with the pumping strength. This entails that both stretching and rotation A_g phonon branches play a role, maintaining a constant ratio in their population during the first stage. Subsequently, during the second stage, V atoms displace mostly along the **c** axis, suggesting the dominant role of the rotational A_g phonon mode. The proportionality of the displacements along the **a** and **c** axis in the fast process [see Fig. 3(a)] can be interpreted as electron excitation by every single photon that does not correlate with neighboring sites, followed by the energy transformation from hot electrons to both stretching and rotation branches of A_g phonon. In contrast, in the second or slow stage, the displacement Δz keeps increasing while Δx remains mostly constant. The second stage dynamics could result from complex phonon-phonon couplings in the thermalization process as well as interaction with strain waves, favoring in aggregate the rotation A_g phonon branch, and reflecting a nonlinear displacement behavior. Based on the trajectory dependence on pump fluence in Fig. 3(c), our observation suggests that the linear part of the trajectory during the first few picoseconds could extend further and reach the R position directly in the first few picoseconds if the pump fluence was sufficiently high.

The observed two-stage relaxation behavior is likely due to strong charge redistribution among the three V t_{2g} orbitals and the nearest V—V and V—O bonds [35] and does not exhibit the characteristic low-energy modes of the R phase. In an unbiased model Hamiltonian, Paquet and Leroux-Hugon predicted [39] that electron-electron

interactions are the leading mechanism of the R-M1 phase transition. This implies that electron-electron interactions in principle could yield different paths of lattice distortions depending on the mutual filling of the V d orbitals. Such a possibility was likely revealed in the second-stage non-thermal process observed in our UED experiments, whereas electron-phonon interactions likely dominate the first stage. To verify this, we performed further density-functional-theory calculations.

The first-principles calculations were done in the generalized gradient approximation (GGA) [40] of DFT by using Vienna *ab initio* simulation package (VASP) [41] with the projector-augmented-wave (PAW) potentials [42,43]. To account for the correlation effects, the GGA + U method with $U = 4.2$ eV and $J = 0.8$ eV was used [44,45]. We performed full lattice relaxation and subsequent phonon and electronic band calculations. The volume of the relaxed lattice is larger by only 0.89% than the experimental value [32]. The calculated difference in the V—V bond lengths is 0.66 Å, compared with the experimental value of 0.55 Å. An $8 \times 8 \times 8$ k mesh in the primitive Brillouin zone and the energy cutoff of 550 eV were used after convergence tests. The harmonic phonon dispersion calculations were performed with VASP and PHONOPY [46], which was found sufficient for the M1 phase [47].

Since the experimental (long-range average) coordinates retain the symmetry of the M1 phase ($P2_1/c$), the atomic displacement is a superposition of the nine Γ -point A_g Raman phonon modes, as shown in Fig. 4(c) and in Fig. S4 in Supplemental Material [27]. Upon projecting the experimental coordinates on phonon eigenvectors, we find that mode 6 dominates the photoexcitation response among A_g modes. The mode-6 phonon frequency is about 6.5 THz (or 27 meV), considerably harder than the lowest phonon energy (~ 2.5 THz) at \mathbf{K}_R for the R phase computed using renormalized effective harmonic force constants from AIMD simulations at $T = 300$ K with nonanalytical term correction, similar to previous reports [18,47]. The atom-resolved (color coded) theoretical phonon bands in the M1 phase are presented in Fig. 4(b). Mode 6 at Γ (blue color) mainly consists of V motions along the **c** axis. In contrast, mode 19 and mode 20 at Γ (red color) consist of V motions along the **a** axis. The time-dependent projected weights of mode 6 and modes 19 and 20 resemble Fig. 3(a). At time zero, the V t_{2g} electrons reside in the x^2-y^2 orbitals and the 800 nm (1.55 eV) laser pump is likely to excite these x^2-y^2 electrons to the electron-band states at 1.55 eV above the ground state [11,13]. Theoretically, the orbital characters of these high-energy states remain elusive, since the conclusion strongly depends on the specific exchange-correlation function adopted in the calculations [47–49]: they can be predominantly of the yz orbital character (which would favor the untwisting of the V-V dimers) or the antibonding x^2-y^2 molecular orbital (which would favor the dimer stretching). Our observation that the V atoms initially move along the M1-R line suggests that a mixture of the yz and

x^2-y^2 orbitals is a more likely scenario, leading to the initial excitation of superimposed A_g modes, which are then relaxed to a mode-6 dominated metastable state surviving 100–800 ps with the other energy dumped to the acoustic phonons [34,36,37].

Some recent studies also reported direct measurements of the electronic structure change upon laser excitation in V_2O_3 , using ultrafast resonant inelastic x-ray scattering (RIXS) [50] and time-resolved photoelectron spectroscopy [51]. Their results showed that the electronic structure changes dramatically within the first few picoseconds. This matches well with the timescale of lattice structure in our measurement. The metallization that was as fast as tens of femtoseconds in ultrafast optical spectroscopy can be attributed to the redistribution of photoexcited electrons in conduction band from the $3d$ valence band. The metallization can be induced by photocarrier doping upon a relatively low pump fluence of $\sim 3\text{--}5\text{ mJ/cm}^2$ [19,25,52]. On the other hand, the electronic structure involving $d-d$ orbital transition strongly correlates with the V-V dimerization change during the photoinduced phase transition, thus taking a longer time.

B. Volume fraction of the R phase during photoexcitation

A long-standing puzzle regarding the VO_2 IMT is the volume fraction of the R phase induced by photoexcitation, especially for experimental probes that are not purely surface sensitive. Our literature search suggests that in most pump-probe x-ray and electron diffraction experiments observations of remaining intensity for the

reflections that solely belong to the M1 phase at above threshold-pump fluences were reported, indicative of an incomplete or inhomogeneous IMT within the probed volume [8,9,19,26,53]. Noticeably, in UED measurements that are sensitive to 10 atomic layers on the surface [9] only around 35% attenuation of M1 peak (606) was observed at the maximum applied pump fluence of 14 mJ/cm^2 . Even at the fluence of 40 mJ/cm^2 in 50-nm-thick polycrystalline films [28] the IMT was clearly incomplete as the intensity of the (-302) reflection, which solely belongs to the M1 phase, only dropped 60%. This agrees with our observation that at 16 mJ/cm^2 the overall intensity of the M1 reflections drops only 35%, especially considering that some probed areas were as thick as 100 nm, which is much harder to be photoexcited. Thus, incomplete attenuation of diffraction peaks of the M1 phase in VO_2 pump-probe experiments is a common phenomenon across reported experiments (see Table S2 in Supplemental Material [27]), unless the samples are warmed very close to the transition temperature before photoexcitation [20,54]. Clearly, the nature of the probe (photons or electrons), the pump fluence and repetition rate, the sample temperature, and the sample thickness related to the pump laser penetration depth and mode of probing (reflection or transmission) can all make a huge difference in the observations [see Fig. 5(a) and Table S2 [27]]. We also note that in previous analyses of diffraction data, reflections belonging to both M1 and R phases were often selected, obfuscating the interpretation. As both electron and x-ray diffraction provide structure information averaged through the probing volume of the sample, there could be the existence of multiple nontrivial transition trajectories and our result represents the most

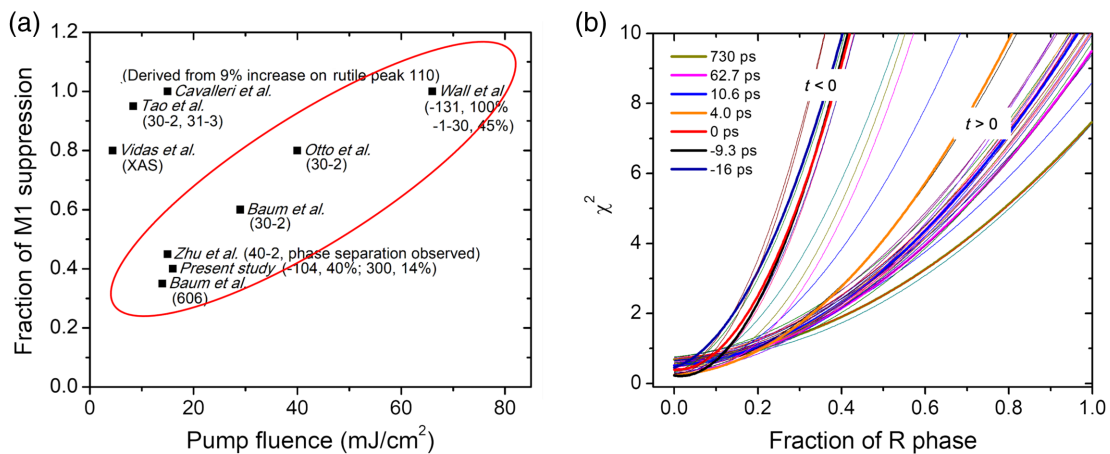


FIG. 5. Exploring the photoinduced volume fraction of the R phase. (a) A comparison of the suppression ratio of the M1 phase reflection intensities after photoexcitation for different pump fluences reported in the literature using ultrafast electrons and x rays. The comparison may not be straightforward as the sample volume and base temperature, which are not included here, might be critical (e.g., data from Ref. [54]). For simplicity, only the most meaningful suppressions are included. For more details, see Table S2 in Supplemental Material [27]. (b) The values of χ^2 derived from Eq. S4 through structure refinement of 20 independent Bragg reflections as a function of the volume fraction of the R phase before and after photon excitation. Data of 42 time delays (thin lines) are included with a few marked by thick lines. The least-squares method was used for the refinement with the parameters such as the displacement along \mathbf{a} and \mathbf{c} direction and the Debye-Waller factors.

likely correlated structural evolution pathway. A more sophisticated and quantitative assessment of the VO₂ response under photoexcitation requires a more careful modeling including the possibility of phase inhomogeneity and quantifying phase fractions within the probed volume.

To resolve these long-standing issues, we quantify the R-phase volume fraction forming upon photoexcitation based on the diffraction intensities measured with MeV UED. We perform a structural refinement including all the candidate phases based on the intensity changes of 20 independent reflections at each time delay under our maximum fluence 16 mJ/cm². Since our single-crystal samples were thinned with FIB, a nonuniform thickness ranging from 20 to 100 nm (with an average thickness of 60 nm) is expected, as shown in Fig. S1(c) [27]. At each time delay after photoexcitation, we assume there are three different volume fractions in the sample. One is a volume in which the IMT was completed, i.e., R phase was reached 100%. The second is a volume where the effect of photoexcitation was negligible, i.e., $\Delta x = \Delta z = 0$ (e.g., regions where pump fluence is below the required threshold due to attenuation along the thickness direction). In these regions, the scattering contribution to the diffracted intensities is also limited as the electron transmission depends exponentially on depth z as $\exp(-z/\text{mfp})$, where mfp is the electron mean-free path. The third volume represents regions of primary interest where photoexcitation partially distorts the M1 phase (denoted below as M1p). Since the diffraction intensity does not change with time in the regions where the effect of photoexcitation is negligible, i.e., $\Delta I_{h0l}^{\text{M1}} = 0$, the relative intensity change of the $h0l$ reflections after photoexcitation can be expressed as $[(\Delta I_{h0l})/(I_{h0l}^0)] = [(p\Delta I_{h0l}^{\text{M1p}} + q\Delta I_{h0l}^{\text{R}})/(I_{h0l}^0)] = p[(\Delta I_{h0l}^{\text{M1p}})/(I_{h0l}^0)] + q[(\Delta I_{h0l}^{\text{R}})/(I_{h0l}^0)]$, where p and q are the volume fractions of M1p and R phases, respectively. The volume fraction of nonexcited M1 phase is $1 - p - q$. Figure 5(b) shows the χ^2 as a function of q for different time delays based on the refinement of 20 Bragg reflections as a function of the volume fraction q of the R phase before and after photon excitation (for details, see Note 7 in Supplemental Material [27]). The χ^2 increases parabolically with q , indicating that the R phase volume fraction is negligible (below 5%) before and after photoexcitation.

We note that the M1p volume fraction (p) is correlated with Δx , Δz , and ΔB , and we only solve $p\Delta x$, $p\Delta z$, and $p\Delta B$ from Eq. S4 (see Note 7 in Supplemental Material [27]). In other words, what can be derived from the experiment data are the displacements and DW averaged over the fractions of distorted (M1p) and undistorted M1 within the probed volume. Because the displacements Δx and Δz scale linearly with p , a small volume fraction of M1p will lead to an underestimation of atomic displacements resulting from photoexcitation. This could likely explain why theoretically calculated photoinduced displacements in VO₂ are often larger than the experimental

observations [33]. The analysis further validates the observed trend for out-of-equilibrium lattice dynamics ($\Delta x/\Delta z$) as shown in Fig. 3, even if the absolute displacement values might be unattainable.

C. Evaluating the possibility of an intermediate M2 phase

Previous studies with Raman microprobe, x-ray diffraction, and electron diffraction proposed that the monoclinic M1 phase can evolve into another insulating monoclinic M2 phase ($C2/m$) under applied strain and temperature variation [30,55–57]. Pump-probe experiments using 60 keV UED on polycrystalline VO₂ films investigated whether photoexcitation could also induce the M1 to M2 transition [20]. Because of the limited diffraction information obtainable from polycrystalline samples, evidence for the existence of an M2 structure in time-resolved measurements remains controversial. Our measurements on single-crystal VO₂ provide a more definite picture of the M1 structural evolution after photoexcitation, in the low excitation regime. Importantly, our MeV pump-probe experiments show no evidence of a transition to the M2 phase within ~ 800 ps after the laser pump. Specifically, we do not observe the emergence of a set of reflections that would be consistent with the ($C2/m$) crystal symmetry characteristic of the M2 phase [58], which, if they did occur, would be located at the positions marked by the green circles in Fig. 1(b) (for detailed analysis, see Fig. S2 [27]). Thus, our results suggest the M2 phase may not be an intermediate phase during the VO₂ IMT below the pump fluence of 16 mJ/cm².

D. Thermal effects

In many ultrafast experiments in VO₂ using short laser pulses as a trigger, a controversy remains over whether thermal or nonthermal photoexcitation effects dominate the induced phase transition [8,19,20,54]. This is in part because the laser energy injected in the system corresponding to the critical fluence initiating the phase transition is nearly equal to the thermal energy required to heat the sample up to the transition temperature. To investigate this point, we repeated our MeV UED measurements with liquid nitrogen cooling and kept the base sample temperature at 77 K under the same pump fluence of 16 mJ/cm². The low repetition rate of 5 Hz in our setup minimizes the residual heating of the sample from pulse to pulse. Somewhat surprisingly, at 77 K, we observe no major suppression of the M1 phase upon photoexcitation (Fig. 6). The intensity evolution of the M1 and R reflections are very similar: they undergo an 8% intensity drop in the first 7 ps and then recover within the subsequent 100 ps, reaching a plateau where the intensity is only 3% less than that before time zero. This dynamic is very distinct from the behavior at 314 K, where the photoinduced distortions in the M1

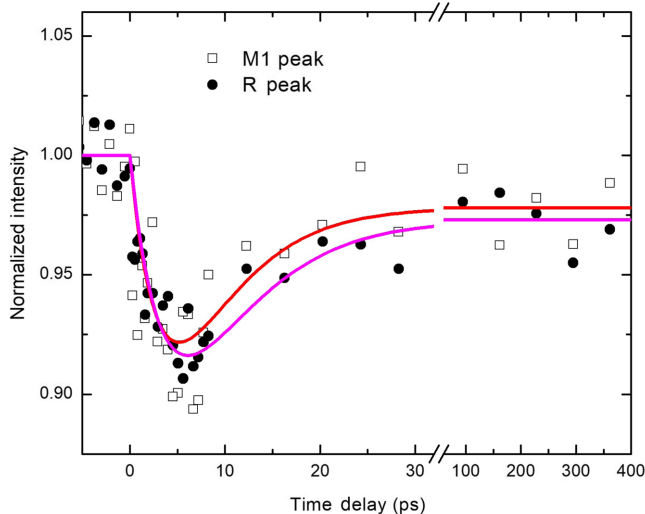


FIG. 6. Intensity evolution of the monoclinic (M1) reflections and the rutile (R) reflections at base sample temperature of 77 K under pump fluence of 16 mJ/cm^2 . Intensity change of both M1 peaks (open square) and R peaks (solid dot) follows a similar pattern with a 10% drop in the first 5 ps and a 7% recovery in the subsequent 30 ps. This is distinctly different from the observations at 314 K [see Fig. 2(a)].

phase toward the R phase transition could be clearly identified by the simultaneous intensity decrease of M1 peaks and increase of R peaks, respectively. The fluence of 16 mJ/cm^2 we use at 314 K is much higher than the threshold required by the phase transition and those reported at room temperature in the literature [9,18,19]. It is unlikely that, under the same pump fluence at 77 K, optical doping would lead to a different perturbation in the electronic state in the system. Recent studies suggest that the threshold for the photoinduced phase transition in VO_2 highly depends on the sample base temperature [20,54,59], despite the arguments that the IMT could be induced with a threshold mostly independent of sample temperature [60]. The obvious difference in our UED measurements at 77 and 314 K indicates the photoinduced M1-R structure phase transition in VO_2 may not be solely driven by a simple melting of the ground-state dimer electronic structure. We attribute the increased phase transition barrier to the alteration of the lattice latent heat or entropy. The M1-R transition requires sufficient optical absorption to overcome the energy barriers related to both structure symmetry breaking and latent heat due to the change of sample base temperature in VO_2 . While thermal heating is shown to be critical to the photoinduced phase transition in VO_2 , its exact role remains not well understood. In many ultrafast studies the absorbed energy from photoexcitation is much higher than the latent heat and specific heat required for the transition; nevertheless, a full M1-R transition is hardly observed. On the other hand, a recent study shows that a pump laser with 2000 nm wavelength can also drive the phase transition and the estimated absorbed energy is far

less than the required thermal energy for the transition, suggesting that the driving force could come from photo-induced electronic structure change [20]. It is noteworthy that recently the phenomenon of orbital degeneracy lifting (ODL) at intermediate temperature, which is not a continuation of the ground-state order but an ODL state with considerably larger entropy, was discovered in a number of multiorbital systems [61–63]; therefore, distinctive responses to laser pumping at different temperature regimes are anticipated. It is thus interesting to probe whether an ODL state exists in VO_2 in future experiments.

VI. SUMMARY

Using MeV UED we have studied the photoinduced structural dynamics of the monoclinic (M1) phase in VO_2 single crystals. We demonstrate that upon photoexcitation the V dimers near-instantaneously start by elongating and concomitantly untwisting in a process that completes in a few picoseconds, while the process of dimer untwisting continues and extends to hundreds of picoseconds. During this deformation process, V atoms start by moving along the direct path from M1 to R phase in the first few picoseconds, and subsequently deviate toward the direction of V-V dimer untwisting. Since the dimer elongation and untwisting can be attributed to the softening of stretching and rotation modes of M1 zone-center A_g phonon modes, the two dynamic behaviors are likely to arise from the difference in coupling strength of various A_g phonons with excited electronic state pumped by the 800 nm photons. The results entail selective phonon excitation that could reflect the intricate electron-lattice coupling, especially the charge redistribution among vanadium t_{2g} orbitals. Our DFT and AIMD calculations suggest that the first stage of the photoinduced lattice distortion in the M1 phase relaxes toward the R phase, in agreement with the present experiment but at odds with some prior reports [9], and that the second-stage lattice distortion mainly follows one A_g Raman phonon mode of the M1 phase. We further address the long-standing issues of the volume fraction of R phase and incomplete IMT induced by photoexcitation and the role of thermal heating under the required, or even well above, pump fluence threshold. It will be intriguing to learn in future studies how the transition path varies under much higher pump fluences, including those that may drive a complete transition to the R phase, if sample damage could be avoided. Our results shed new light on the understanding of IMT and photoinduced electronic and lattice dynamics in VO_2 .

ACKNOWLEDGMENTS

This work was mainly supported by the Materials Science and Engineering Divisions, Office of Basic Energy Sciences of the U.S. Department of Energy under Contract No. DESC0012704. J. T. was supported by a U.S.

DOE Early Career Award. X. J. acknowledges support from the visiting research scholarship of Brookhaven National Laboratory and the support of National Natural Science Foundation of China (No. 11774119). S. Y. acknowledges support by the Fitzpatrick Institute for Photonics through a Chambers Scholarship. O. D. acknowledges support from the U.S. Department of Energy, Office of Science, Basic Energy Sciences, Materials Sciences and Engineering Division, under Award No. DE-SC0019978.

-
- [1] D. N. Basov, R. D. Averitt, and D. Hsieh, *Towards Properties on Demand in Quantum Materials*, *Nat. Mater.* **16**, 1077 (2017).
- [2] D. Fausti, R. I. Tobey, N. Dean, S. Kaiser, A. Dienst, M. C. Hoffmann, S. Pyon, T. Takayama, H. Takagi, and A. Cavalleri, *Light-Induced Superconductivity in a Stripe-Ordered Cuprate*, *Science* **331**, 189 (2011).
- [3] R. Mankowsky, A. Subedi, M. Först, S. O. Mariager, M. Chollet, H. T. Lemke, J. S. Robinson, J. M. Glownia, M. P. Miniti, A. Frano, M. Fechner, N. A. Spaldin, T. Loew, B. Keimer, A. Georges, and A. Cavalleri, *Nonlinear Lattice Dynamics as a Basis for Enhanced Superconductivity in $\text{YBa}_2\text{Cu}_3\text{O}_{6.5}$* , *Nature (London)* **516**, 71 (2014).
- [4] N. Aryal, X. Jin, Q. Li, A. M. Tsvelik, and W. Yin, *Topological Phase Transition and Phonon-Space Dirac Topology Surfaces in ZrTe_5* , *Phys. Rev. Lett.* **126**, 016401 (2021).
- [5] C. Vaswani, L. L. Wang, D. H. Mudiyansele, Q. Li, P. M. Lozano, G. D. Gu, D. Cheng, B. Song, L. Luo, R. H. J. Kim, C. Huang, Z. Liu, M. Mootz, I. E. Perakis, Y. Yao, K. M. Ho, and J. Wang, *Light-Driven Raman Coherence as a Nonthermal Route to Ultrafast Topology Switching in a Dirac Semimetal*, *Phys. Rev. X* **10**, 021013 (2020).
- [6] S. Nie, X. Wang, H. Park, R. Clinite, and J. Cao, *Measurement of the Electronic Grüneisen Constant Using Femtosecond Electron Diffraction*, *Phys. Rev. Lett.* **96**, 025901 (2006).
- [7] M. Eichberger, H. Schäfer, M. Krumova, M. Beyer, J. Demsar, H. Berger, G. Moriena, G. Sciaini, and R. J. D. Miller, *Snapshots of Cooperative Atomic Motions in the Optical Suppression of Charge Density Waves*, *Nature (London)* **468**, 799 (2010).
- [8] A. Cavalleri, C. Tóth, C. W. Siders, J. A. Squier, F. Ráksi, P. Forget, and J. C. Kieffer, *Femtosecond Structural Dynamics in VO_2 during an Ultrafast Solid-Solid Phase Transition*, *Phys. Rev. Lett.* **87**, 237401 (2001).
- [9] P. Baum, D.-S. Yang, and A. H. Zewail, *4D Visualization of Transitional Structures in Phase Transformations by Electron Diffraction*, *Science* **318**, 788 (2007).
- [10] P. Zhu, Y. Zhu, Y. Hidaka, L. Wu, J. Cao, H. Berger, J. Geck, R. Kraus, S. Pjetrov, Y. Shen, R. I. Tobey, J. P. Hill, and X. J. Wang, *Femtosecond Time-Resolved MeV Electron Diffraction*, *New J. Phys.* **17**, 063004 (2015).
- [11] J. Li, W.-G. Yin, L. Wu, P. Zhu, T. Konstantinova, J. Tao, J. Yang, S.-W. Cheong, F. Carbone, J. A. Misewich, J. P. Hill, X. Wang, R. J. Cava, and Y. Zhu, *Dichotomy in Ultrafast Atomic Dynamics as Direct Evidence of Polaron Formation in Manganites*, *npj Quantum Mater.* **1**, 16026 (2016).
- [12] T. Konstantinova, J. D. Rameau, A. H. Reid, O. Abdurazakov, L. Wu, R. Li, X. Shen, G. Gu, Y. Huang, L. Rettig, I. Avigo, M. Ligges, J. K. Freericks, A. F. Kemper, H. A. Dürr, U. Bovensiepen, P. D. Johnson, X. Wang, and Y. Zhu, *Non-equilibrium Electron and Lattice Dynamics of Strongly Correlated $\text{Bi}_2\text{Sr}_2\text{CaCu}_2\text{O}_{8+d}$ Single Crystals*, *Sci. Adv.* **4**, eaap7427 (2018).
- [13] T. Konstantinova, L. Wu, W. G. Yin, J. Tao, G. D. Gu, X. J. Wang, J. Yang, I. A. Zaliznyak, and Y. Zhu, *Photoinduced Dirac Semimetal in ZrTe_5* , *npj Quantum Mater.* **5**, 80 (2020).
- [14] M. Nakano, K. Shibuya, D. Okuyama, T. Hatano, S. Ono, M. Kawasaki, Y. Iwasa, and Y. Tokura, *Collective Bulk Carrier Delocalization Driven by Electrostatic Surface Charge Accumulation*, *Nature (London)* **487**, 459 (2012).
- [15] K. Liu, D. Fu, J. Cao, J. Suh, K. X. Wang, C. Cheng, D. F. Ogletree, H. Guo, S. Sengupta, A. Khan, C. W. Yeung, S. Salahuddin, M. M. Deshmukh, and J. Wu, *Dense Electron System from Gate-Controlled Surface Metal-Insulator Transition*, *Nano Lett.* **12**, 6272 (2012).
- [16] K. Liu, S. Lee, S. Yang, O. Delaire, and J. Wu, *Recent Progresses on Physics and Applications of Vanadium Dioxide*, *Mater. Today* **21**, 875 (2018).
- [17] Z. Shao, X. Cao, H. Luo, and P. Jin, *Recent Progress in the Phase-Transition Mechanism and Modulation of Vanadium Dioxide Materials*, *NPG Asia Mater.* **10**, 581 (2018).
- [18] S. Wall, S. Yang, L. Vidas, M. Chollet, J. M. Glownia, M. Kozina, T. Katayama, T. Henighan, M. Jiang, T. A. Miller, D. A. Reis, L. A. Boatner, O. Delaire, and M. Trigo, *Ultrafast Disorder of Vanadium Dimers in Photoexcited VO_2* , *Science* **362**, 572 (2018).
- [19] V. R. Morrison, R. P. Chatelain, K. L. Tiwari, A. Hendaoui, A. Bruhács, M. Chaker, and B. J. Siwick, *A Photoinduced Metal-like Phase of Monoclinic VO_2 Revealed by Ultrafast Electron Diffraction*, *Science* **346**, 445 (2014).
- [20] Z. Tao, F. Zhou, T.-R. T. Han, D. Torres, T. Wang, N. Sepulveda, K. Chang, M. Young, R. R. Lunt, and C.-Y. Ruan, *The Nature of Photoinduced Phase Transition and Metastable States in Vanadium Dioxide*, *Sci. Rep.* **6**, 38514 (2016).
- [21] J. B. Goodenough, *The Two Components of the Crystallographic Transition in VO_2* , *J. Solid State Chem.* **3**, 490 (1971).
- [22] N. F. Mott, *Metal-Insulator Transition*, *Rev. Mod. Phys.* **40**, 677 (1968).
- [23] V. Eyert, *The Metal-Insulator Transitions of VO_2 : A Band Theoretical Approach*, *Ann. Phys. (Amsterdam)* **11**, 650 (2002).
- [24] A. Zylbersztein and N. F. Mott, *Metal-Insulator Transition in Vanadium Dioxide*, *Phys. Rev. B* **11**, 4383 (1975).
- [25] D. Wegkamp, M. Herzog, L. Xian, M. Gatti, P. Cudazzo, C. L. McGahan, R. E. Marvel, R. F. Haglund, A. Rubio, M. Wolf, and J. Stähler, *Instantaneous Band Gap Collapse in Photoexcited Monoclinic VO_2 due to Photocarrier Doping*, *Phys. Rev. Lett.* **113**, 216401 (2014).
- [26] Y. Zhu, Z. Cai, P. Chen, Q. Zhang, M. J. Highland, I. W. Jung, D. A. Walko, E. M. Dufresne, J. Jeong, M. G. Samant, S. S. P. Parkin, J. W. Freeland, P. G. Evans, and H. Wen,

- Mesoscopic Structural Phase Progression in Photo-Excited VO₂ Revealed by Time-Resolved X-Ray Diffraction Microscopy*, *Sci. Rep.* **6**, 21999 (2016).
- [27] See Supplemental Material at <http://link.aps.org/supplemental/10.1103/PhysRevX.12.021032> for additional TEM characterization of the sample, crystal structure parameters, complementary data analysis, and theoretical calculation results.
- [28] M. R. Otto, L. P. René de Cotret, D. A. Valverde-Chavez, K. L. Tiwari, N. Émond, M. Chaker, D. G. Cooke, and B. J. Siwick, *How Optical Excitation Controls the Structure and Properties of Vanadium Dioxide*, *Proc. Natl. Acad. Sci. U.S.A.* **116**, 450 (2019).
- [29] J. Galy and G. Miehe, *Ab Initio Structures of (M2) and (M3) VO₂ High Pressure Phases*, *Solid State Sci.* **1**, 433 (1999).
- [30] J. M. Atkin, S. Berweger, E. K. Chavez, M. B. Raschke, J. Cao, W. Fan, and J. Wu, *Strain and Temperature Dependence of the Insulating Phases of VO₂ Near the Metal-Insulator Transition*, *Phys. Rev. B* **85**, 020101(R) (2012).
- [31] J. M. Zuo and J. C. H. Spence, *Advanced Transmission Electron Microscopy* (Springer New York, 2017).
- [32] J. M. Longo, P. Kierkegaard, C. J. Ballhausen, U. Ragnarsen, S. E. Rasmussen, E. Sunde, and N. A. Sørensen, *A Refinement of the Structure of VO₂*, *Acta Chem. Scand.* **24**, 420 (1970).
- [33] X. Yuan, W. Zhang, and P. Zhang, *Hole-Lattice Coupling and Photoinduced Insulator-Metal Transition in VO₂*, *Phys. Rev. B* **88**, 035119 (2013).
- [34] E. Beaurepaire, J. C. Merle, A. Daunois, and J. Y. Bigot, *Ultrafast Spin Dynamics in Ferromagnetic Nickel*, *Phys. Rev. Lett.* **76**, 4250 (1996).
- [35] Z. He and A. J. Millis, *Photoinduced Phase Transitions in Narrow-Gap Mott Insulators: The Case of VO₂*, *Phys. Rev. B* **93**, 115126 (2016).
- [36] X. Tong and M. Bernardi, *Toward Precise Simulations of the Coupled Ultrafast Dynamics of Electrons and Atomic Vibrations in Materials*, *Phys. Rev. Research* **3**, 023072 (2021).
- [37] L. Waldecker, R. Bertoni, R. Ernstorfer, and J. Vorberger, *Electron-Phonon Coupling and Energy Flow in a Simple Metal beyond the Two-Temperature Approximation*, *Phys. Rev. X* **6**, 021003 (2016).
- [38] X. Wang, J. C. Ekström, Å. U. J. Bengtsson, A. Jarnac, A. Jurgilaitis, V.-T. Pham, D. Kroon, H. Enquist, and J. Larsson, *Role of Thermal Equilibrium Dynamics in Atomic Motion during Nonthermal Laser-Induced Melting*, *Phys. Rev. Lett.* **124**, 105701 (2020).
- [39] D. Paquet and P. Leroux-Hugon, *Electron Correlations and Electron-Lattice Interactions in the Metal-Insulator, Ferroelastic Transition in VO₂: A Thermodynamical Study*, *Phys. Rev. B* **22**, 5284 (1980).
- [40] J. P. Perdew, K. Burke, and M. Ernzerhof, *Generalized Gradient Approximation Made Simple*, *Phys. Rev. Lett.* **77**, 3865 (1996).
- [41] G. Kresse and J. Furthmüller, *Efficient Iterative Schemes for Ab Initio Total-Energy Calculations Using a Plane-Wave Basis Set*, *Phys. Rev. B* **54**, 11169 (1996).
- [42] G. Kresse and D. Joubert, *From Ultrasoft Pseudopotentials to the Projector Augmented-Wave Method*, *Phys. Rev. B* **59**, 1758 (1999).
- [43] P. E. Blöchl, *Projector Augmented-Wave Method*, *Phys. Rev. B* **50**, 17953 (1994).
- [44] D. Plašienka, R. Martoňák, and M. C. Newton, *Ab Initio Molecular Dynamics Study of the Structural and Electronic Transition in VO₂*, *Phys. Rev. B* **96**, 054111 (2017).
- [45] A. Liebsch, H. Ishida, and G. Bihlmayer, *Coulomb Correlations and Orbital Polarization in the Metal-Insulator Transition of VO₂*, *Phys. Rev. B* **71**, 085109 (2005).
- [46] A. Togo, F. Oba, and I. Tanaka, *First-Principles Calculations of the Ferroelastic Transition between Rutile-Type and CaCl₂-Type SiO₂ at High Pressures*, *Phys. Rev. B* **78**, 134106 (2008).
- [47] J. D. Budai, J. Hong, M. E. Manley, E. D. Specht, C. W. Li, J. Z. Tischler, D. L. Abernathy, A. H. Said, B. M. Leu, L. A. Boatner, R. J. McQueeney, and O. Delaire, *Metallization of Vanadium Dioxide Driven by Large Phonon Entropy*, *Nature (London)* **515**, 535 (2014).
- [48] Z. Zhu and U. Schwingenschlögl, *Comprehensive Picture of VO₂ from Band Theory*, *Phys. Rev. B* **86**, 075149 (2012).
- [49] X. Yuan, Y. Zhang, T. A. Abteu, P. Zhang, and W. Zhang, *VO₂: Orbital Competition, Magnetism, and Phase Stability*, *Phys. Rev. B* **86**, 235103 (2012).
- [50] S. Parchenko *et al.*, *Orbital Dynamics during an Ultrafast Insulator to Metal Transition*, *Phys. Rev. Research* **2**, 023110 (2020).
- [51] G. Lantz, B. Mansart, D. Grieger, D. Boschetto, N. Nilforoushan, E. Papalazarou, N. Moisan, L. Perfetti, V. L. R. Jacques, D. Le Bolloc'h, C. Laulhé, S. Ravy, J.-P. Rueff, T. E. Glover, M. P. Hertlein, Z. Hussain, S. Song, M. Chollet, M. Fabrizio, and M. Marsi, *Ultrafast Evolution and Transient Phases of a Prototype Out-of-Equilibrium Mott-Hubbard Material*, *Nat. Commun.* **8**, 13917 (2017).
- [52] C. Kübler, H. Ehrke, R. Huber, R. Lopez, A. Halabica, R. F. Haglund, and A. Leitenstorfer, *Coherent Structural Dynamics and Electronic Correlations during an Ultrafast Insulator-to-Metal Phase Transition in VO₂*, *Phys. Rev. Lett.* **99**, 116401 (2007).
- [53] A. X. Gray *et al.*, *Ultrafast Terahertz Field Control of Electronic and Structural Interactions in Vanadium Dioxide*, *Phys. Rev. B* **98**, 045104 (2018).
- [54] L. Vidas, D. Schick, E. Martínez, D. Perez-Salinas, A. Ramos-Álvarez, S. Cichy, S. Batlle-Porro, A. S. Johnson, K. A. Hallman, R. F. Haglund, and S. Wall, *Does VO₂ Host a Transient Monoclinic Metallic Phase?*, *Phys. Rev. X* **10**, 031047 (2020).
- [55] J. P. Pouget, H. Launois, J. P. D'Haenens, P. Merenda, and T. M. Rice, *Electron Localization Induced by Uniaxial Stress in Pure VO₂*, *Phys. Rev. Lett.* **35**, 873 (1975).
- [56] A. Tselev, I. A. Luk'Yanchuk, I. N. Ivanov, J. D. Budai, J. Z. Tischler, E. Strelcov, A. Kolmakov, and S. V. Kalinin, *Symmetry Relationship and Strain-Induced Transitions between Insulating M1 and M2 and Metallic R Phases of Vanadium Dioxide*, *Nano Lett.* **10**, 4409 (2010).
- [57] J. H. Park, J. M. Coy, T. Serkan Kasirga, C. Huang, Z. Fei, S. Hunter, and D. H. Cobden, *Measurement of a Solid-State Triple Point at the Metal-Insulator Transition in VO₂*, *Nature (London)* **500**, 431 (2013).
- [58] I. P. Zibrov, V. P. Filonenko, V. A. Sidorov, and S. G. Lyapin, *V_{3,047}O₇, a New High-Pressure Oxide with the Simpsonite Structure*, *Inorg. Mater.* **52**, 902 (2016).

- [59] A. Pashkin, C. Kübler, H. Ehrke, R. Lopez, A. Halabica, R. F. Haglund, R. Huber, and A. Leitenstorfer, *Ultrafast Insulator-Metal Phase Transition in VO₂ Studied by Multi-terahertz Spectroscopy*, *Phys. Rev. B* **83**, 195120 (2011).
- [60] T. L. Cocker, L. V. Titova, S. Fourmaux, G. Holloway, H. C. Bandulet, D. Brassard, J. C. Kieffer, M. A. El Khakani, and F. A. Hegmann, *Phase Diagram of the Ultrafast Photo-induced Insulator-Metal Transition in Vanadium Dioxide*, *Phys. Rev. B* **85**, 155120 (2012).
- [61] R. J. Koch, R. Sinclair, M. T. McDonnell, R. Yu, M. Abeykoon, M. G. Tucker, A. M. Tsvetik, S. J. L. Billinge, H. D. Zhou, W. G. Yin, and E. S. Bozin, *Dual Orbital Degeneracy Lifting in a Strongly Correlated Electron System*, *Phys. Rev. Lett.* **126**, 186402 (2021).
- [62] L. Yang, R. J. Koch, H. Zheng, J. F. Mitchell, W. Yin, M. G. Tucker, S. J. L. Billinge, and E. S. Bozin, *Two-Orbital Degeneracy Lifted Local Precursor to a Metal-Insulator Transition in MgTi₂O₄*, *Phys. Rev. B* **102**, 235128 (2020).
- [63] E. S. Bozin, W. G. Yin, R. J. Koch, M. Abeykoon, Y. S. Hor, H. Zheng, H. C. Lei, C. Petrovic, J. F. Mitchell, and S. J. L. Billinge, *Local Orbital Degeneracy Lifting as a Precursor to an Orbital-Selective Peierls Transition*, *Nat. Commun.* **10**, 3638 (2019).